Science Bulletin xxx (xxxx) xxx

Contents lists available at ScienceDirect

Science Bulletin

journal homepage: www.elsevier.com/locate/scib

Article

Observation of miniaturized bound states in the continuum with ultra-high quality factors

Zihao Chen [a], Xuefan Yin [a], Jicheng Jin [b], Zhao Zheng [a], Zixuan Zhang [a], Feifan Wang [a], Li He [b], Bo Zhen [b], Chao Peng [a,c,*]

[a] State Key Laboratory of Advanced Optical Communication Systems and Networks, Department of Electronics & Frontiers Science Center for Nano-optoelectronics, Peking University, Beijing 100871, China
[b] Department of Physics and Astronomy, University of Pennsylvania, Philadelphia, PA 19104, USA
[c] Peng Cheng Laboratory, Shenzhen 518055, China

ARTICLE INFO

Article history:
Received 23 August 2021
Received in revised form 11 October 2021
Accepted 13 October 2021
Available online xxxx

Keywords:
Bound state in the continuum
Photonic crystal
High-Q cavity
Topological photonics

ABSTRACT

Light trapping is a constant pursuit in photonics because of its importance in science and technology. Many mechanisms have been explored, including the use of mirrors made of materials or structures that forbid outgoing waves, and bound states in the continuum that are mirror-less but based on topology. Here we report a compound method, combining lateral mirrors and bound states in the continuum in a cooperative way, to achieve a class of on-chip optical cavities that have high quality factors and small modal volumes. Specifically, light is trapped in the transverse direction by the photonic band gap of the lateral hetero-structure and confined in the vertical direction by the constellation of multiple bound states in the continuum. As a result, unlike most bound states in the continuum found in photonic crystal slabs that are de-localized Bloch modes, we achieve light-trapping in all three dimensions and experimentally demonstrate quality factors as high as $Q = 1.09 \times 10^6$ and modal volumes as low as $V = 17.74(\lambda_0/n)^3$ in the telecommunication regime. We further prove the robustness of our method through the statistical study of multiple fabricated devices. Our work provides a new method of light trapping, which can find potential applications in photonic integration, nonlinear optics and quantum computing.

1. Introduction

While most light-trapping methods rely on the use of mirrors to forbid radiation [1–6], it is recently realized that optical bound states in the continuum (BICs) provide an alternative approach [7–12]. BICs are localized wave functions with energies embedded in the radiation continuum, but, counter-intuitively, do not couple to the radiation field. Since their initial proposal [13], BICs have been demonstrated in multiple wave systems, including photonic [7,8], phononic [14], acoustic [15], and water waves [16], and have found important applications in lasers [17–19], filters [20], sensors [21], nonlinear optics [19,22–25], and quantum devices [26,27]. In many cases, BICs can be understood as topological defects [28–32]: for example, they are fundamentally vortices in the far field polarization in photonic crystal (PhC) slabs, each carrying an integer topological charge [33]. Manipulations of these topological charges have led to interesting consequences, including resonances that become more robust to scattering losses [11] and unidirectional guided resonances that only radiate towards a single side without the use of mirrors on the other [34].

So far, most BICs studied in PhC slabs are only localized in the vertical (thickness) direction, but remain de-localized in the transverse direction across the slab, rendering them less ideal in enhancing light-matter interaction with localized emitters [35], nonlinear optics [22–24], or quantum applications [27]. While it is known that in theory perfect BICs localized in all three dimensions cannot exist [36], it is of great interest and practical importance exploring the limit of BIC miniaturization, namely to what extent the model volumes of BICs can be shrunk while preserving their high-Q characteristics. A simple truncation of the PhC slab can reduce modal volume V, but also drastically degrades the quality factor Q, as it introduces leakage in both lateral and vertical directions. A common relationship between Q and V for BICs with outgoing boundary conditions in plane has been derived [37], showing good agreements with experiments [38]. As a recent example [39], quasi-BIC with Q of 18,511 has been observed in a truncated

* Corresponding author.
E-mail address: pengchao@pku.edu.cn (C. Peng).

https://doi.org/10.1016/j.scib.2021.10.020
2095-9273/

metasurface of 19 × 19 μm^2, and a Q of 7300 was demonstrated in InGaAsP PhC slab for low-threshold lasing in footprint of 22.4 × 22.4 μm^2 [40]. On the other hand, the truncation can also be achieved by applying lateral hetero-structure as reflective perimeter. However, although the hetero-structure forbids transverse leakage, the leakage in vertical direction upon the whole PhC region remains unresolved, thus limiting the Qs, accordingly, as Q of only 2.0 × 10^4 has been measured in footprint of 215 μm^2 [25,41].

Here we theoretically propose and experimentally demonstrate a method to achieve miniaturized BICs (mini-BICs) in PhC slabs, through the proper arrangement of multiple topological charges in the momentum space, along with the use of lateral reflective mirrors. Specifically, we start by enclosing the mini-BIC with a photonic band-gap mirror, using a lateral hetero-structure, to forbid transverse leakage. Similar to electronic quantum dots, the continuous photonic bands of an infinite PhC turn into discrete energy levels, due to the momentum quantization determined by the size of the mini-BIC. For the same reason, the out-of-plane leakage of the mini-BIC predominantly happens in the few specific directions which satisfy the momentum-quantization condition. As the PhC unit cell design is varied, multiple BICs [7,8,42,43]— each carrying a topological charge and together composing a topological constellation — evolve in the momentum space, and eventually match with the major leakage channels. At this point, the out-of-plane radiation of the mini-BIC is topologically eliminated, leading to an ultra-long photon lifetime and a small modal volume at the same time.

2. Methods

2.1. Numerical simulation

All simulations are performed using the COMSOL Multiphysics in the frequency domain. Three-dimensional models are created with photonic crystal slabs placed between two perfect-matching layers. In other words, we have periodic boundary condition in-plane and out-going boundary condition in the vertical direction. The spatial meshing resolution is adjusted to adequately capture resonances with Qs of up to 10^9. The eigenvalue solver is used to compute the frequencies and the quality factors of the resonances. The far-field emission patterns are computed by first retrieving the complex electric fields $\mathbf{E}_{0,j}$ ($j = x,\ y$) just above the PhC surface and then calculating the emission fields as [38]:

$$F_j(\theta,\phi) \propto (\cos\theta + \cos\phi - 1)\int\int_{x,y} E_{0,j}(x,y)e^{-ik_0(\tan\theta x+\tan\phi y)}\mathrm{d}x\mathrm{d}y. \quad (1)$$

The modal volume of a cavity mode refers to the following formula [44]:

$$V = \frac{\int \varepsilon(\boldsymbol{r})|\mathbf{E}(\boldsymbol{r})|^2\mathrm{d}^3\boldsymbol{r}}{\max[\varepsilon(\boldsymbol{r})|\mathbf{E}(\boldsymbol{r})|^2]} \quad (2)$$

where $\varepsilon(\boldsymbol{r})$ is the material dielectric constant, and $|\mathbf{E}(\boldsymbol{r})|$ is the electric field strength. V can be normalized to $(\lambda_0/n)^3$, where λ_0 is the wavelength in vacuum and n is the refractive index of the PhC slab [2].

2.2. Sample fabrication

We fabricate the sample on a silicon-on-insulator (SOI) wafer with e-beam lithography (EBL) and then with induced coupled plasma (ICP) etching. For EBL, we first spin-coat the cleaved SOI chips with a 500 nm-thick layer of ZEP520A photo-resist before it is exposed with EBL (JBX-9500FS) at beam current of 400 pA and field size of 500 μm. Then we etch the sample with ICP (Oxford Plasmapro Estrelas 100) using a mixture of SF_6 and CHF_3. After etching, we remove the resist with N-Methyl-2-pyrrolidone (NMP) and the buried oxide layer using 49% HF.

2.3. Measurement setup

We use a tunable laser (Santec TSL-550, C + L band) to generate incident light. The light is first sent through a polarizer (Y-Pol) and is focused by a lens (L1) onto the rear focal plane of an objective (Mitutoyo Apo NIR, 50X). The reflected and scattered light is collected by the same objective and a 4f system is used to adjust the magnification ratio to 2.67X to best fit the observation. After passing through an orthogonal polarizer (X-Pol), only the scattered light is collected using a photo-diode (PDA10DT-EC). The resonance peaks are recorded by a high-speed data acquisition card (NI PCIe-6361) connected to the photo-diode during wavelength scanning, and then fitted to Lorentzian function. A flip mirror is used to switch between the camera (PI NIRvana) and photodetector, in order to record the x-polarized far-field pattern of each mode. The y-polarized far-field pattern can similarly be obtained by switching the two polarizers (Y-Pol/X-Pol) to their orthogonal polarized directions (X-Pol/Y-Pol), respectively. Then we obtain the overall far-field pattern by combining the x- and y-polarized patterns together. Besides characterizing far-field patterns, the setup could also switch to near-field observation if another lens is inserted between L2 and L3.

3. Design and topological interpretation

As a specific example, we have designed a PhC slab (Fig. 1a), where circular air holes (radius $r = 175$ nm) are defined in a silicon layer of $h = 600$ nm thick. The mini-BIC design consists of a square cavity region A surrounded by a boundary region B with a gap size of $g = 541$ nm between them. Each side of the cavity region A has the same length of L. Region A and B have different periodicities, $a = 529$ nm and $b = 552$ nm, to form a hetero-structure in-plane (see the Supplementary materials Part I for the detailed design). We focus on the lowest-frequency TE band in region A above the light line (black line in Fig. 1b), whose energy is embedded in the band-gap of region B that forbids lateral leakage. As elaborated in the Supplementary materials Part II and III, such lateral mirror also causes scattering loss at the hetero-structure interface due to momentum-mismatch, and radiation loss from boundary region B as the loss itself resides in the radiation continuum. By tuning parameters b and g, the interface between region A and B turns to be almost perfectly reflective, minimizing the transverse leakage of the mini-BIC.

In a finite sized structure encircled by a square perimeter, the continuous band of a PhC (left panel of Fig. 1b) splits into a series of discrete modes (right-panel) as the continuous momentum space is quantized into isolated points with a spacing of $\delta k = \pi/L$ (Fig. 1c). This is analogous to what happens in an electronic quantum dot. Each mode can thus be labeled by a pair of integers ($p,\ q$), indicating that its momentum is mostly localized near ($p\pi/L,\ q\pi/L$) in the first quadrant (see the Supplementary materials Part IV for the detailed analytical theory of momentum quantization). Four modes, M_{11} through M_{22}, are shown as examples, where M_{12} and M_{21} are degenerate in frequency due to the 90-degree rotation symmetry of the structure (C_4). The quantized momenta lead to distinctly different near- and far-field patterns of these finite size modes (Fig. 1d) that agree well with the theory (Fig. S5 online). By applying the definition of modal volume V,

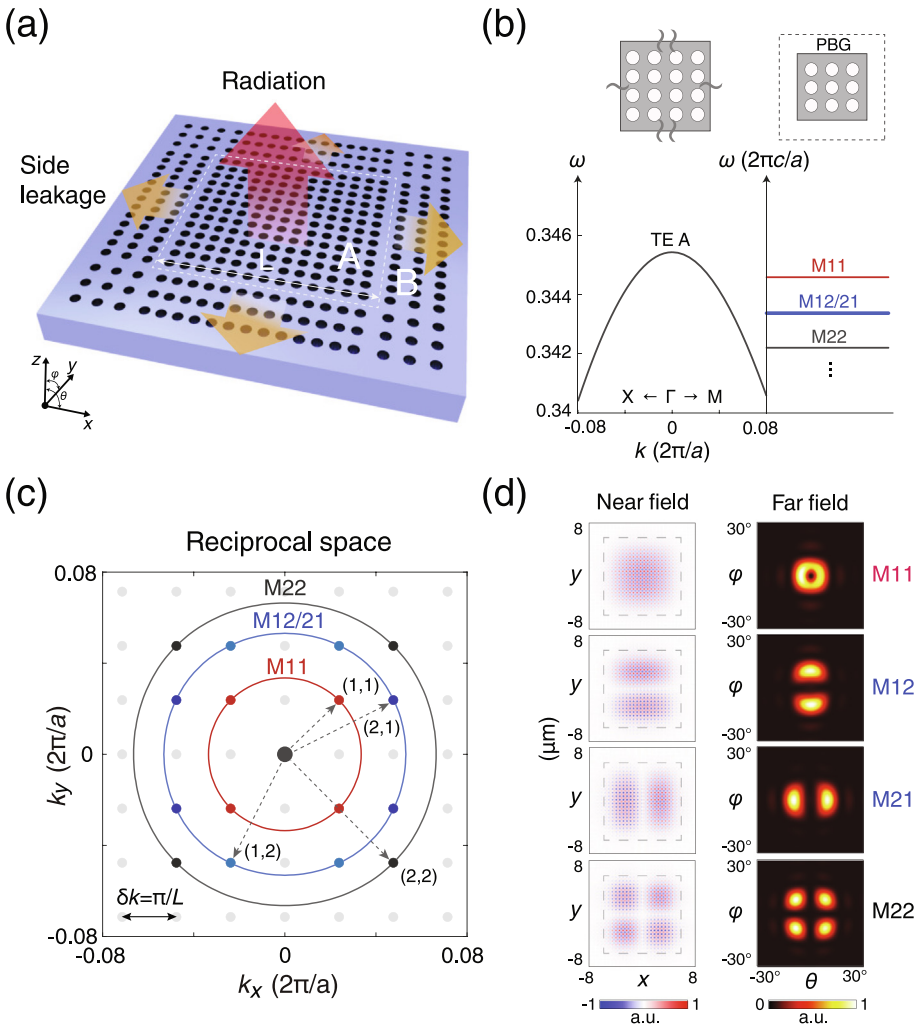

Fig. 1. (Color online) Mini-BIC modes. (a) Schematic of a mini-BIC (region A) surrounded a photonic bandgap (PBG, region B). (b) A continuous band (TE-A) of an infinitely large PhC with periodic boundary condition (left) turns into a set of discrete modes under the PBG boundary condition (right). (c) The momentum distribution of each mode is highly localized to points that form a square lattice in the momentum space with a spacing of π/L. Modes are labeled as M_{pq}, according to their momentum peak positions in the first quadrant at $(p\pi/L, q\pi/L)$. (d) The near-field mode profiles of four modes M_{11} through M_{21}(left) and their far-field emission patterns (right).

the *Vs* of M_{11}, $M_{12/21}$ and M_{22} are calculated as $17.74(\lambda_0/n)^3$, $16.61(\lambda_0/n)^3$ and $15.90(\lambda_0/n)^3$, respectively (see Methods for more details). It is noteworthy that, owing to momentum-quantization, we found that the out-of-plane radiation is in fact dominated by a few specific directions that are off the exact vertical normal, if the lateral mirror is assumed as almost perfectly reflective (see the Supplementary materials Part II–V for more details).

Next, we show that the radiation loss of each mode can be strongly suppressed through the topological constellation of BICs. Fundamentally, BICs are topological defects in the far-field polarization, which carry integer topological charges:

$$q = \oint_C d\mathbf{k} \cdot \nabla_{\mathbf{k}} \phi(\mathbf{k}). \tag{3}$$

Here $\phi(\mathbf{k})$ is the angle between the polarization major axis of radiation from the mode at $\mathbf{k}$ and the *x*-axis. *C* is a simple closed path that goes around the BIC in the counter-clockwise (CCW) direction. As shown in Fig. 2a, for an infinite PhC with $a = 526.8$ nm (case *W*), there are 9 BICs: one is at the center of the Brillouin zone (BZ), and the others form an octagonal-shaped topological constellation, which is denoted by their distance to the BZ center (k_{BIC}). The position of the topological constellation can be controlled by varying the periodicity *a*: for example, as *a* increases from 526.8 nm (case *W* in Fig. 2a) to 534 nm (case *Z*), the topological constellation shrinks and merges together before it turns into a single topological charge. The evolution of the *Q*s of infinite PhCs is shown in the lower panel of Fig. 2a. Note that case *Y* corresponds to our previously reported "merging BICs" in infinite PhC [11], in which radiation towards normal direction is topologically suppressed.

Since the radiation in finite size structure is directional but off the normal, whenever the topological constellation matches with the main momenta of a mode M_{pq}, i.e., $k_{BIC}L/\pi = \sqrt{p^2+q^2}$, its radiation loss is strongly suppressed, as its major underlying Bloch mode components are now BICs with infinitely high *Q*s. This is confirmed by our simulation results in Fig. 2b (see Methods for more details): the *Q* of M_{11} (red line) is maximized in case *X* when the matching condition is met. The maximum *Q* exceeds 8×10^6. Similarly, the *Q*s of M_{12} (blue) and M_{22} (black) are also maximized when their matching conditions are satisfied, labelled by blue and black dashed lines, respectively. Here we note that all localized modes penetrate, partly, into the boundary region, so the effective cavity length L_{eff} is calculated as $22.3a$, which is slightly larger than the physical length of the cavity $L = 17a$. Accordingly, the theory and simulations agree well with each other (see the Supplemen-

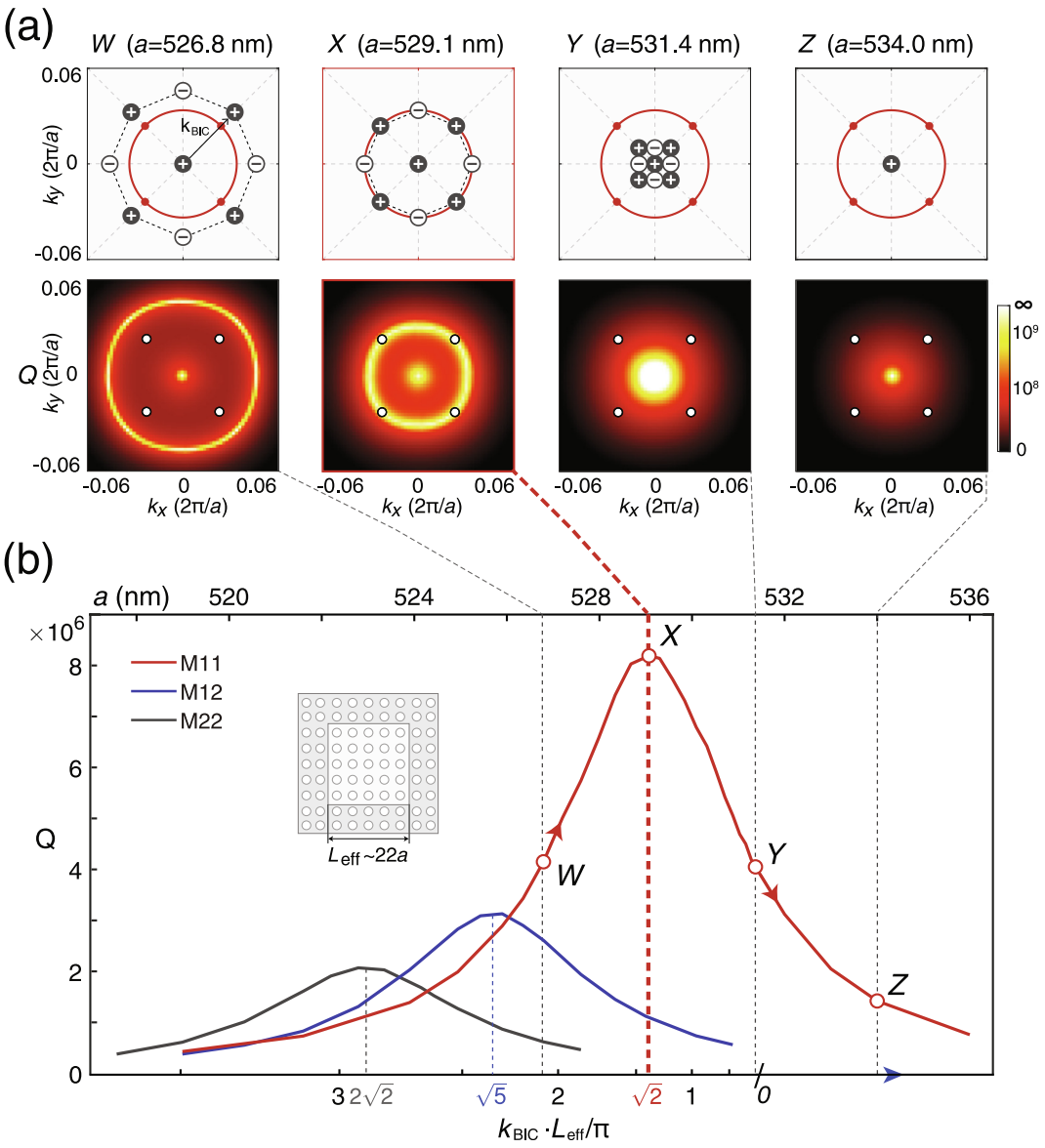

Fig. 2. Maximizing the *Q*s of mini-BICs by properly arranging topological charges in the momentum space. (a) Multiple BICs appear on bulk band TE-A in momentum space, in which 8 off-Γ ones with $q = \pm 1$ topological charges compose an octagonal-shaped topological constellation, denoted by the radius k_{BIC}. When unit cell periodicity a varies from 526.8 nm (W) to 534.0 nm (Z), the topological constellation shrinks, merges, and annihilates to a single topological charge (upper panel). The quality factor Q for each unit cell design is shown in the lower panel. (b) The quality factor Q of modes, M_{11} through M_{22}, as functions of periodicity a (upper axis) and topological constellation k_{BIC} (lower axis). Q for M_{11} (red line) maximizes when its quantized momentum $\sqrt{2}\pi/L$ matches the topological constellation k_{BIC}, corresponding to case X ($a = 529.1$ nm) in (a). Similar maxima are also observed for M_{12} (blue) and M_{22} (black) under other designs, when k_{BIC} matches $\sqrt{5}\pi/L$ and $2\sqrt{2}\pi/L$, respectively.

tary materials Part VI for more details), which indicates that the optimal *Q*s of mini-BICs depend on the cavity length L and modal quantum number (p, q), but not simply at the "merging BIC" design of case *Y*.

4. Sample fabrication and experimental setup

To verify our theoretical findings, we fabricate PhC samples using e-beam lithography and induced coupled plasma etching processes on a 600 nm thick silicon-on-insulator wafer (see Methods for more details on the fabrication). The scanning electron microscope (SEM) images of the samples are shown in Fig. 3. The underlying SiO_2 layer is removed before measurements to restore the up–down mirror symmetry, required by the off-normal BICs. The footprint of the each sample is about 19.8 μm × 19.8 μm, including a cavity region that is 11.9 μm × 11.9 μm in size. The periodicity of the cavity region a is varied from 518 to 534 nm to satisfy the matching-condition and maximize *Q*s of M_{11}, M_{12} and M_{22}. The periodicity of the boundary region and the gap distance are fixed at $b = 552$ nm and $g = 541$ nm. Since fabrication inevitably brings structural imperfections and disorders, such as side-wall tilting and fluctuation of air-holes, we estimated the titled angle of sidewall is $\sim 0.6^{\circ}$, and the standard deviation of air-hole centers is about 4.2 nm from the SEM images of the samples.

The experimental setup is schematically shown in Fig. 3d, which is similar to our previously reported results [11,34]. A tunable laser in the telecommunication band is first sent through a polarizer in the *y*-direction (POL Y) before it is focused by a lens (L1) onto the rear focal plane (RFP) of an infinity-corrected objective lens. In order to maximize the coupling efficiency, we fine-tune L1 so that the incident angle of the laser is aligned to the radiation direction of cavity

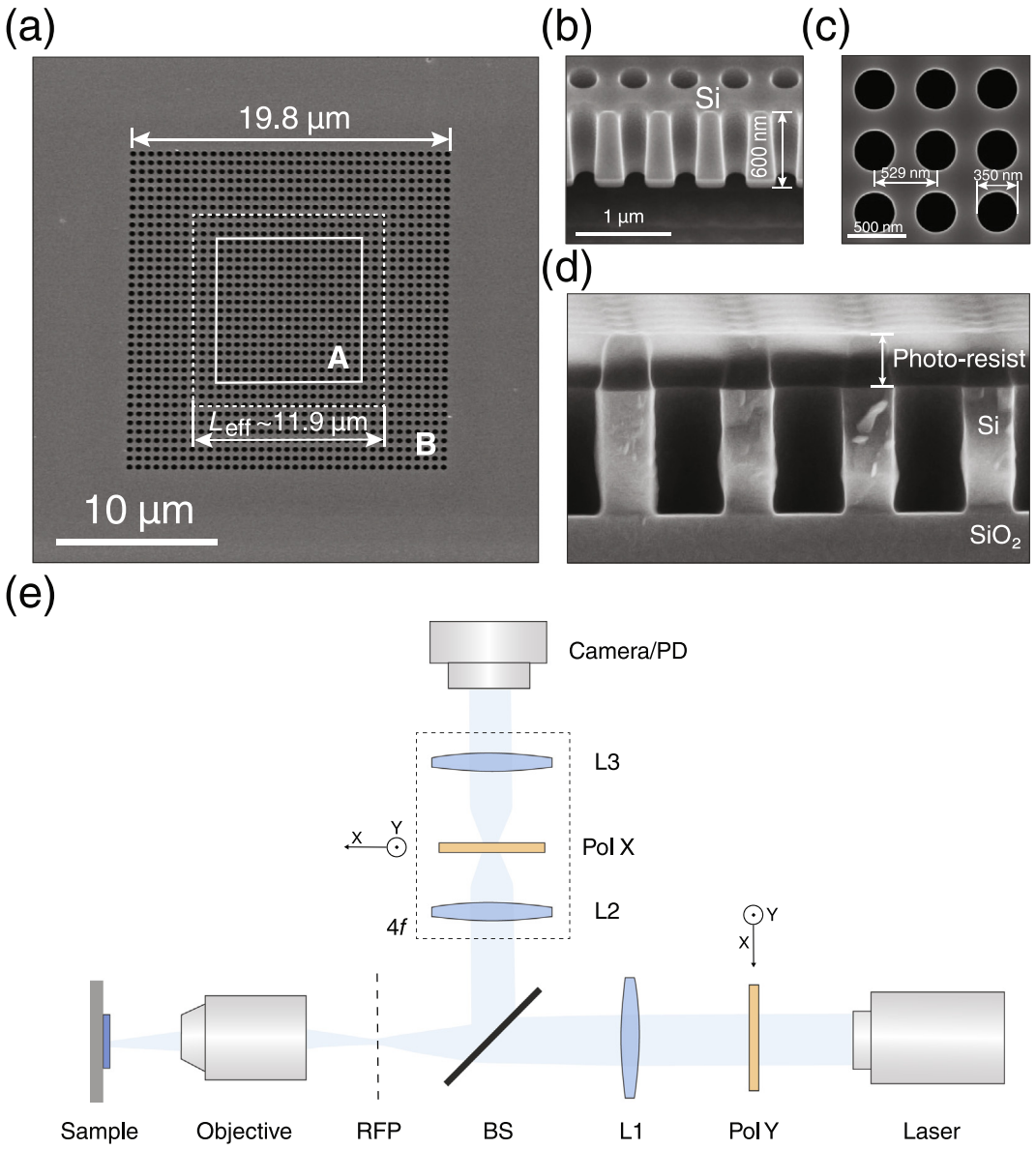

Fig. 3. Fabricated sample and experimental setup. (a–d) Scanning electron microscope images of the fabricated samples from top and side views. The photoresist and underlying SiO_2 layer are removed before measurements. The chosen structural parameters correspond to case X in Fig. 2a to maximize Q for mode M_{11}. (e) Schematic of the experimental setup. L, lens; RFP, real focal plane; PD, photodiode; POL, polarizer; BS, beam-splitter; Lens L2 and L3 are confocal.

mode, at the same time, ensuring the beam diameter to be matched with the cavity region in real space. The reflected beam is collected by the same objective, and further expanded by 2.67 times through a 4*f* system to best fit the camera. Since the direct reflected light remains as *y*-polarized but the resonance's radiation possesses both *x*- and *y*-polarized components, a *x*-direction (Pol X) is used to block direct reflection from the sample, while allowing the resonance's radiation to pass. As a result, the resonances gain better signal–noise-ratio for observation and exhibit symmetric Lorentzian features. Furthermore, by placing a pin hole at the image plane of the RFP of the objective to reject stray light, light intensity from resonance's radiation is recorded using a photo-diode as the wavelength of the tunable laser is scanned. See Methods for more details on the experimental setup.

5. Experimental results

Whenever the excitation laser wavelength becomes on-resonance with a mini-BIC mode, the scattered light from the sample, captured on the camera, is maximized, which allows us to measure the resonance frequencies and *Q*s of different modes. Furthermore, under on-resonance condition, the far-field radiation pattern of each mode can also be recorded by the camera with polarizers (Fig. 4a): we first record the *x*-polarized pattern under "*y*-polarized incident and *x*-polarized detection"; then change the polarizer setting to "*x*-polarized incident and *y*-polarized detection" to record the *y*-polarized pattern accordingly; finally, we obtain the overall far-field pattern by combining the *x*- and *y*-polarized patterns together. The far-field radiation of mode M_{11}, M_{12} and M_{22} is measured to be donut-, dipole- and quadrupole-shaped, respectively, showing good agreements with numerical simulation and theory. By scanning the wavelength, distinct and sharp resonance peaks are found (mid-panel in Fig. 4b), corresponding to the 4 modes, M_{11} through M_{22}. We note that the fabrication imperfection slightly breaks the C_4 symmetry and causes a minimal energy difference (≈0.03%) between M_{12} and M_{21}.

Higher resolution measurements near each mode yield results shown in the left and right panels of Fig. 4b. The design is

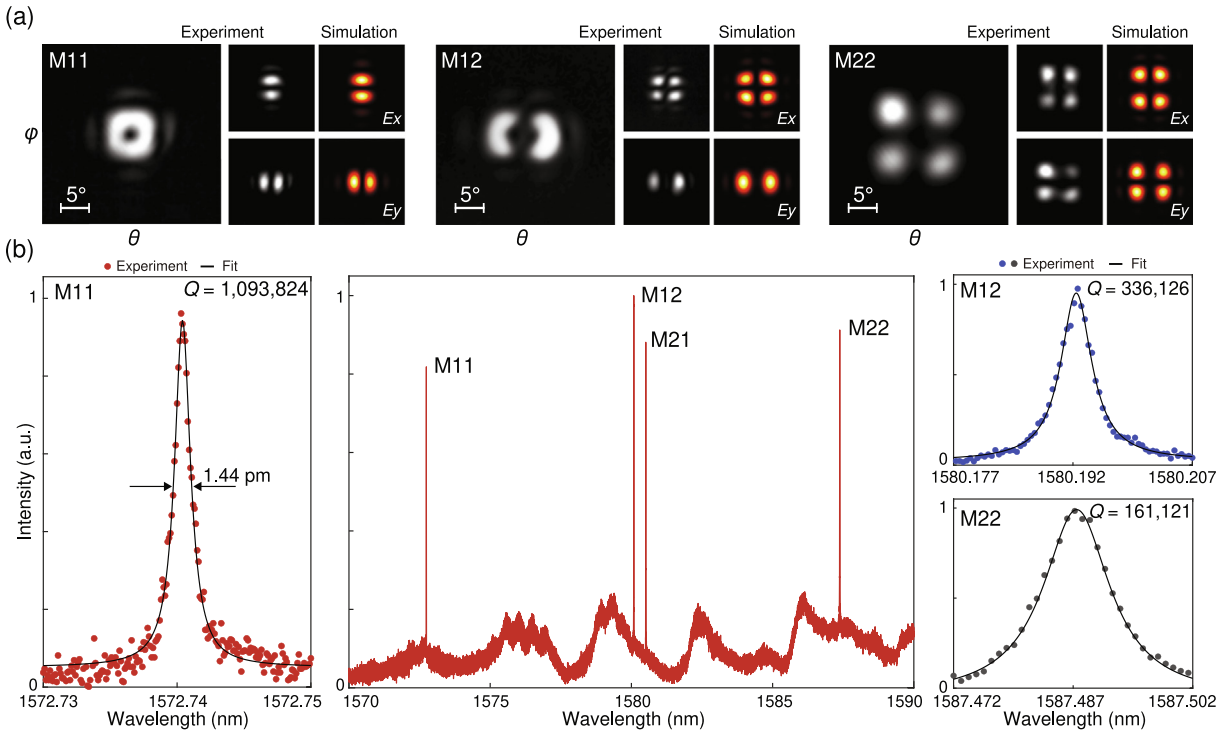

Fig. 4. Observation of mini-BIC modes. (a) The far-field emission patterns (x/y-polarized and overall) of modes M_{11} through M_{22}, measured with a camera (gray color map), show good agreements with simulation results (hot color map). (b) Middle panel: measured scattered light intensity as the laser wavelength scans from 1570 to 1590 nm. Four clear peaks are observed and identified as M_{11} through M_{22}. The Q of M_{11} reaches 1.09×10^6 (left panel). In the same sample, the Qs of M_{12} and M_{22} are measured as 3.36×10^5 and 1.61×10^5, respectively (right panel).

optimized for mode M_{11} ($a = 529$ nm). The Q of each mode is extracted by numerically fitting the scattering spectrum to a Lorentzian function. As is shown, the measured Qs of modes M_{12} and M_{22} are 3.36×10^5 and 1.61×10^5, respectively. Meanwhile, the highest Q for mode M_{11} reaches 1.09×10^6, corresponding to a full width half maximum of 1.44 pm. Comparing with our reported results of merging BICs [11], the observed mini-BIC is 150-fold shrinking of footprint (from 250×250 μm to 20×20 μm) with 2-fold enhancement of Q (from 4.9×10^5 to 1.09×10^6). While comparing with the BICs in truncated structures of similar footprint [39], the mini-BIC exhibits 50-fold enhancement of measured Q ($\sim 2.0 \times 10^4$ to 1.09×10^6). Therefore we conclude that the proposed mini-BIC indeed achieves light-trapping in all three dimensions.

Furthermore, to demonstrate the suppression of radiation loss originated from topological constellation, we vary periodicity a between 518 and 534 nm and track how Q changes. The measured wavelength of all modes agree well with simulation results (Fig. 5a). We see that, indeed, their measured Qs are always maximized when the topological-constellation-matching condition is met, which happens when $a = 529.1$, 525.9, and 522.8 nm for M_{11}, M_{12} and M_{22}, respectively, but not at the merging BIC condition of $a = 531.4$ nm (Fig. 5b). This finding shows good agreement with our simulation results in Fig. 2b. Finally, we prove the robustness of our method by measuring 87 different samples fabricated

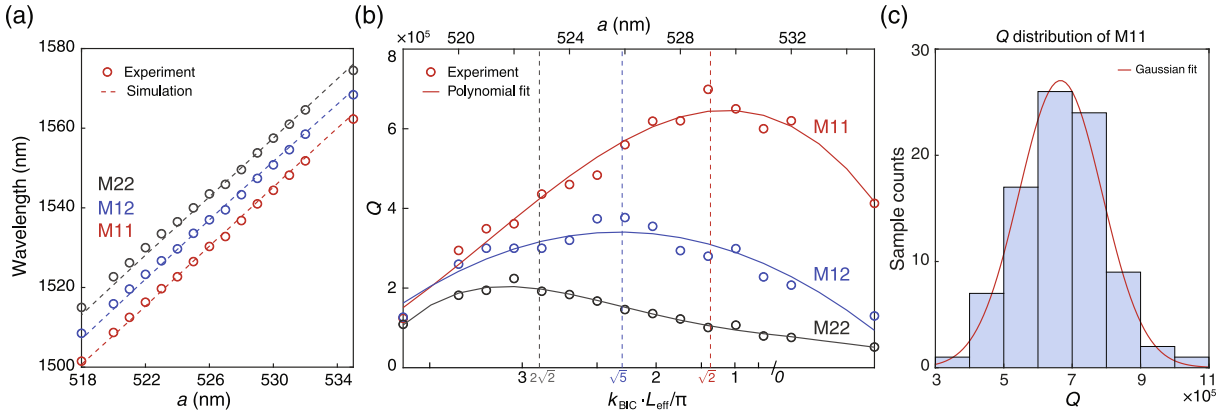

Fig. 5. Demonstration of mini-BIC robustness against fabrication errors. (a) Measured resonance wavelengths (circles) in samples with different periodicities a show good agreements with simulation results (dashed lines). (b) Measured Qs (circles) in samples with different periodicities a (upper axis) and, therefore, different topological constellation (k_{BIC}, lower axis). Polynomial fittings are shown in solid lines. Each curve is maximized when the matching condition is satisfied, indicated as dashed vertical lines. (c) Histogram statistics of measured Qs of M_{11} in 87 samples, showing the robustness of our mini-BICs.

under the same design and through the same process. The histogram of their measured Qs of mode M_{11} is shown in Fig. 5c, featuring an averaged Q of 6.65×10^5 with a modest standard deviation of 1.22×10^5. See the Supplementary materials Part VII for more details.

When transversely trapping light into small volume, in-plane momenta are quantized into isolated points and out-of-plane radiation turns to be directional. Therefore the radiation can be strongly suppressed by topological-constellation-matching. This mechanism relies on a cooperative arrangement of lateral mirror and topological constellation. Although simple photonic band gap mirror is applied in this work, we expect with optimism that other mechanisms for transverse localization of light, such as interface between trivial and topological regions [12,45], or moiré photonic lattices [46–48], can achieve the same effect. The more mini-BICs shrink, the more the radiation deviates from vertical normal, which renders the difference between topological-constellation-matching condition and merging-BIC. Nevertheless, the mini-BICs also partially benefit from the asymptotic behaviour of bulk $Q \propto 1/[k(k+k_{BIC})(k-k_{BIC})]^2$ to against out-of-plane scattering, if the matched wavevector $k_{BIC} = \sqrt{p^2+q^2} \cdot \pi/L$ is not extremely large, namely the cavity size L is not extremely small. The potentials of mini-BICs in smaller V and higher Q, as well as other relevant discussions are presented in the Supplementary materials Part VIII–X.

To summarize, we present a type of ultra-high-Q and ultra-compact mini-BICs by combining in-plane mirrors and out-of-plane BICs in a cooperative way. We experimentally demonstrate a record-high quality factor for BICs of $Q = 1.09 \times 10^6$ and a small modal volume of $17.74(\lambda_0/n)^3$, that is 3.56 μm^3. Our finding can potentially lead to on-chip lasers with ultra-low thresholds [49–51], chemical or biological sensors [21,52–54], nonlinear nanophotonic devices [22–24], and elements for quantum computing [26,55,56]. Furthermore, our method of achieving ultra-high-Q and ultra-low-V are proven to be robust, owing to their topological nature, which paves the way to further improving the performance of optoelectronic devices [18,49,57,58].

Conflict of interest

The authors declare that they have no conflict of interest.

Acknowledgments

This work was partly supported by the National Natural Science Foundation of China (61922004 and 62135001), National Key Research and Development Program of China (2020YFB1806405), the Major Key Project of PCL (PCL2021A14), the Open Fund of the State Key Laboratory of Integrated Optoelectronics, US National Science Foundation through the University of Pennsylvania Material Research Science and Engineering Center (DMR-1720530), US Office of Naval Research (ONR) Multidisciplinary University Research Initiative (MURI) Grant N00014-20-1-2325 on Robust Photonic Materials with High-Order Topological Protection and the US Army Research Office under award contract W911-NF-19–1-0087. The simulation of this work was supported by High-performance Computing Platform of Peking University.

Author contributions

Chao Peng conceived the idea. Zihao Chen, Xuefan Yin, Li He, Bo Zhen and Chao Peng performed the theoretical study. Zihao Chen, Jicheng Jin, Xuefan Yin, and Chao Peng performed the analytical calculations and numerical simulations. Zihao Chen, Zhao Zheng, Zixuan Zhang and Feifan Wang conducted the experiments and analyzed the data. Zihao Chen, Xuefan Yin, Jicheng Jin, Bo Zhen and Chao Peng wrote the manuscript, with input from all authors. Chao Peng supervised the research. All authors contributed to the discussions of the results.

Appendix A. Supplementary materials

Supplementary materials to this article can be found online at https://doi.org/10.1016/j.scib.2021.10.020.

References

[1] Akahane Y, Asano T, Song BS, et al. High-Q photonic nanocavity in a two-dimensional photonic crystal. Nature 2003;425:944–7.
[2] Song BS, Noda S, Asano T, et al. Ultra-high-Q photonic double-heterostructure nanocavity. Nat Mater 2005;4:207–10.
[3] Lu X, Lee JY, Feng PXL, et al. High Q silicon carbide microdisk resonator. Appl Phys Lett 2014;104:181103.
[4] Biberman A, Shaw MJ, Timurdogan E, et al. Ultralow-loss silicon ring resonators. Opt Lett 2012;37:4236–8.
[5] Vahala KJ. Optical microcavities. Nature 2003;424:839–46.
[6] Srinivasan K, Borselli M, Painter O, et al. Cavity Q, mode volume, and lasing threshold in small diameter algaas microdisks with embedded quantum dots. Opt Express 2006;14:1094.
[7] Hsu CW, Zhen B, Lee J, et al. Observation of trapped light within the radiation continuum. Nature 2013;499:188–91.
[8] Lee J, Zhen B, Chua SL, et al. Observation and differentiation of unique high-Q optical resonances near zero wave vector in macroscopic photonic crystal slabs. Phys Rev Lett 2012;109:067401.
[9] Bulgakov EN, Maksimov DN. Topological bound states in the continuum in arrays of dielectric spheres. Phys Rev Lett 2017;118:267401.
[10] Hsu CW, Zhen B, Stone AD, et al. Bound states in the continuum. Nat Rev Mater 2016;1:16048.
[11] Jin J, Yin X, Ni L, et al. Topologically enabled ultrahigh-Q guided resonances robust to out-of-plane scattering. Nature 2019;574:501–4.
[12] Gao X, Yang L, Lin H, et al. Dirac-vortex topological cavities. Nat Nanotechnol 2020;15:1012–8.
[13] von Neuman J, Wigner E. Uber merkwürdige diskrete eigenwerte. uber das verhalten von eigenwerten bei adiabatischen prozessen. Physikalische Zeitschrift 1929;30:467–70.
[14] Tong H, Liu S, Zhao M, et al. Observation of phonon trapping in the continuum with topological charges. Nat Commun 2020;11:5216.
[15] Cumpsty NA, Whitehead DS. The excitation of acoustic resonances by vortex shedding. J Sound Vib 1971;18:353–69.
[16] Cobelli PJ, Pagneux V, Maurel A, et al. Experimental observation of trapped modes in a water wave channel. EPL 2009;88:20006.
[17] Meier M, Mekis A, Dodabalapur A, et al. Laser action from two-dimensional distributed feedback in photonic crystals. Appl Phys Lett 1998;74:7–9.
[18] Hirose K, Liang Y, Kurosaka Y, et al. Watt-class high-power, high-beam-quality photonic-crystal lasers. Nat Photonics 2014;8:406–11.
[19] Koshelev K, Kruk S, Melik-Gaykazyan E, et al. Subwavelength dielectric resonators for nonlinear nanophotonics. Science 2020;367:288–92.
[20] Foley JM, Young SM, Phillips JD. Symmetry-protected mode coupling near normal incidence for narrow-band transmission filtering in a dielectric grating. Phys Rev B 2014;89:165111.
[21] Zhen B, Chua SL, Lee J, et al. Enabling enhanced emission and low-threshold lasing of organic molecules using special fano resonances of macroscopic photonic crystals. Proc Natl Acad Aci USA 2013;110:13711–6.
[22] Soljačić M, Joannopoulos JD. Enhancement of nonlinear effects using photonic crystals. Nat Mater 2004;3:211–9.
[23] Carletti L, Koshelev K, De Angelis C, et al. Giant nonlinear response at the nanoscale driven by bound states in the continuum. Phys Rev Lett 2018;121:033903.
[24] Bernhardt N, Koshelev K, White SJ, et al. Quasi-bic resonant enhancement of second-harmonic generation in WS_2 monolayers. Nano Lett 2020;20:5309–14.
[25] Minkov M., Gerace D., Fan S. Doubly resonant $\chi^{(2)}$ nonlinear photonic crystal cavity based on a bound state in the continuum. Optica 2019;6:1039–1045.
[26] Hacker B, Welte S, Rempe G, et al. A photon–photon quantum gate based on a single atom in an optical resonator. Nature 2016;536:193–6.
[27] Sun S, Kim H, Luo Z, et al. A single-photon switch and transistor enabled by a solid-state quantum memory. Science 2018;361:57–60.
[28] Kitamura K, Sakai K, Takayama N, et al. Focusing properties of vector vortex beams emitted by photonic-crystal lasers. Opt Lett 2012;37:2421–3.
[29] Iwahashi S, Kurosaka Y, Sakai K, et al. Higher-order vector beams produced by photonic-crystal lasers. Opt Express 2011;19:11963–8.
[30] Zhang Y, Chen A, Liu W, et al. Observation of polarization vortices in momentum space. Phys Rev Lett 2018;120:186103.
[31] Doeleman HM, Monticone F, den Hollander W, et al. Experimental observation of a polarization vortex at an optical bound state in the continuum. Nat Photonics 2018;12:397.

[32] Lu L, Joannopoulos JD, Soljačić M. Topological photonics. Nat Photonics 2014;8:821–9.
[33] Zhen B, Hsu CW, Lu L, et al. Topological nature of optical bound states in the continuum. Phys Rev Lett 2014;113:257401.
[34] Yin X, Jin J, Soljačić M, et al. Observation of topologically enabled unidirectional guided resonances. Nature 2020;580:467–71.
[35] Perczel J, Borregaard J, Chang DE, et al. Topological quantum optics using atomlike emitter arrays coupled to photonic crystals. Phys Rev Lett 2020;124:083603.
[36] Silveirinha MG. Trapping light in open plasmonic nanostructures. Phys Rev A 2014;89:023813.
[37] Chua SL, Chong Y, Stone AD, et al. Low-threshold lasing action in photonic crystal slabs enabled by fano resonances. Opt Express 2011;19:1539.
[38] Liang Y, Peng C, Sakai K, et al. Three-dimensional coupled-wave analysis for square-lattice photonic crystal surface emitting lasers with transverse-electric polarization: Finite-size effects. Opt Express 2012;20:15945–61.
[39] Liu Z, Xu Y, Lin Y, et al. High-*Q* quasibound states in the continuum for nonlinear metasurfaces. Phys Rev Lett 2019;123:253901.
[40] Hwang MS, Lee HC, Kim KH, et al. Ultralow-threshold laser using super-bound states in the continuum. Nat Commun 2021;12:4135.
[41] Wang J, Clementi M, Minkov M, et al. Doubly resonant second-harmonic generation of a vortex beam from a bound state in the continuum. Optica 2020;7:1126–32.
[42] Ni L, Wang Z, Peng C, et al. Tunable optical bound states in the continuum beyond in-plane symmetry protection. Phys Rev B 2016;94:245148.
[43] Yang Y, Peng C, Liang Y, et al. Analytical perspective for bound states in the continuum in photonic crystal slabs. Phys Rev Lett 2014;113:037401.
[44] Akahane Y, Asano T, Song BS, et al. Fine-tuned high-*Q* photonic-crystal nanocavity. Opt Express 2005;13:1202–14.
[45] Shao ZK, Chen HZ, Wang S, et al. A high-performance topological bulk laser based on band-inversion-induced reflection. Nat Nanotechnol 2020;15:67–72.
[46] Fu Q, Wang P, Huang C, et al. Optical soliton formation controlled by angle twisting in photonic moiré lattices. Nat Photonics 2020;14:663–8.
[47] Wang P, Zheng Y, Chen X, et al. Localization and delocalization of light in photonic moiré lattices. Nature 2020;577:42–6.
[48] Tang H, Du F, Carr S, et al. Modeling the optical properties of twisted bilayer photonic crystals. Light Sci Appl 2021;10:157.
[49] Ellis B, Mayer MA, Shambat G, et al. Ultralow-threshold electrically pumped quantum-dot photonic-crystal nanocavity laser. Nat Photonics 2011;5:297–300.
[50] Wu S, Buckley S, Schaibley JR, et al. Monolayer semiconductor nanocavity lasers with ultralow thresholds. Nature 2015;520:69–72.
[51] Yao P, Rao VSCM, Hughes S. On-chip single photon sources using planar photonic crystals and single quantum dots. Laser Photonics Rev 2010;4:499–516.
[52] Romano S, Zito G, Torino S, et al. Label-free sensing of ultralow-weight molecules with all-dielectric metasurfaces supporting bound states in the continuum. Photonics Res 2018;6:726–33.
[53] Yanik AA, Cetin AE, Huang M, et al. Seeing protein monolayers with naked eye through plasmonic fano resonances. Proc Natl Acad Sci 2011;108:11784–9.
[54] Chen W, Kaya Özdemir Ş, Zhao G, et al. Exceptional points enhance sensing in an optical microcavity. Nature 2017;548:192–6.
[55] Liu J, Zhu KD. Single-photon controlled switch based on the giant kerr nonlinearity in the single-spin coupled to levitated nanodiamonds. Opt Commun 2019;450:236–40.
[56] Choi H, Heuck M, Englund D. Self-similar nanocavity design with ultrasmall mode volume for single-photon nonlinearities. Phys Rev Lett 2017;118:223605.
[57] Tanabe T, Notomi M, Kuramochi E, et al. Trapping and delaying photons for one nanosecond in an ultrasmall high-*Q* photonic-crystal nanocavity. Nat Photonics 2007;1:49–52.
[58] Münzberg J, Vetter A, Beutel F, et al. Superconducting nanowire single-photon detector implemented in a 2*d* photonic crystal cavity. Optica 2018;5:658–65.

Zihao Chen received bachelor degree from Southeast University in 2014 and master degree from Peking University in 2016. He is currently a Ph.D. candidate at School of EECS in Peking University. His research interest focuses on mechanisms and applications of high-*Q* photonic crystal cavity.

Chao Peng received his B.S. degree from Department of Physics, Peking University in 2004, and Ph.D. degree from Department of Electronics, Peking University in 2009. He worked at Kyoto University as JSPS Fellowship from 2009 to 2012. He has joined Department of Electronic, Peking University since 2012 and his current position is an associated professor. His research interest includes topological photonics, non-Hermitian photonics and photonic integration.